

RSC Advances



This is an *Accepted Manuscript*, which has been through the Royal Society of Chemistry peer review process and has been accepted for publication.

Accepted Manuscripts are published online shortly after acceptance, before technical editing, formatting and proof reading. Using this free service, authors can make their results available to the community, in citable form, before we publish the edited article. This *Accepted Manuscript* will be replaced by the edited, formatted and paginated article as soon as this is available.

You can find more information about *Accepted Manuscripts* in the [Information for Authors](#).

Please note that technical editing may introduce minor changes to the text and/or graphics, which may alter content. The journal's standard [Terms & Conditions](#) and the [Ethical guidelines](#) still apply. In no event shall the Royal Society of Chemistry be held responsible for any errors or omissions in this *Accepted Manuscript* or any consequences arising from the use of any information it contains.

Roles of Hydrogen bond and π - π stacking in the optic detection of nitro-explosives with luminescent metal organic framework as sensor

Lei Liu,^{a,b} Juanyuan Hao,^a Yantao Shi,^a Jieshan Qiu^a and Ce Hao^{*a}

ABSTRACT With the aids of density functional theory (DFT) and time-dependent density functional theory (TD-DFT), the explosives-detection mechanism of a typical luminescent metal-organic framework (MOF) sensor has been comprehensively studied by investigating the interactions between the framework and two analytes, namely, benzene and nitrobenzene. By studying both the periodic crystal models and cluster models we obtained an in-depth understanding of the detecting mechanism from the view of electronic coupling between the analyte and sensor. Intermolecular electron transfer from conduction bands of the framework to LUMO of nitrobenzene is demonstrated to be the inducement for the luminescence quenching phenomenon observed in the previous experiment. π - π stacking interaction and hydrogen bonding interaction are found to play essential roles in this intermolecular electron transfer process. π - π stacking provides large fragment orbital overlaps between the unoccupied orbitals of the analyte and sensor, which serves as the high efficient electron transfer bridge. Hydrogen bond, alone, cannot provide enough overlaps for electron transfer but is found to reinforce the π - π stacking interaction. The cooperation of the two interactions induces facile intermolecular electron transfer which strongly quenches the luminescence of the MOF sensor. This work sheds light on the analyte-sensor interactions inside the MOF sensors and would provide valuable insights into the design of high efficient explosives-detecting MOF sensors.

Introduction

Due to the high surface area, strong mechanical stability, extraordinary porosity and designable architecture,¹⁻⁵ metal-organic frameworks (MOFs) have emerged as a new group of promising candidates in molecular storage,⁶⁻⁹ gas separation,¹⁰⁻¹² drug delivery,¹³ and catalysis.¹⁴⁻¹⁶ Some MOFs exhibit tunable electrical and optical properties which enable them to be potential candidates such as active materials for hybrid solar cells, quantum dots, and organic semiconducting devices.¹⁷⁻²⁷ Herein, the studies of the optical properties for MOF materials are of special interest. Moreover, the coordination of metal centers with emissive organic-ligands always render MOFs useful luminescent properties such as high luminescence quantum yield, large stroke shift and guest molecule based emission spectrum changing.²⁸⁻³¹ The combination of their unique structural properties with their multiple optic characteristics endorses MOFs to be platforms for sensing applications.³²⁻³⁴ Their pore windows and the chemical environments inside can be delicately tuned by selecting the proper metal ions and ligands. This will primarily eliminate the relatively bulky interferential molecules and pre-concentrate the analytes. Consequently, the guest-host interaction is optimized which influences the luminescence of the framework and achieves specific analyte detection. Based on this, many luminescent MOFs (LMOFs) have been synthesized for the detections of metal cations, anions and small molecules, making MOFs the research frontier in optic sensors.³²⁻³⁴

One of the most significant application amongst is their ability for sensing nitroaromatics,³⁵ which plays a crucial role in anti-terrorism and homeland security. Since the pioneering work of Li,⁴⁰ dozens of new frameworks have been designed and synthesized for explosives-detection purposes.³⁶⁻⁴⁸ Versatile metal centers and organic-ligands make it possible to design numerous LMOFs for explosives-detection purposes, which is an apparent advantage for MOF-based sensors. However, this kind of versatility also makes it hard for one to select the judicious building blocks from the vast collection of candidates to achieve specific analyte detection. Thus, a clear understanding of the detecting mechanism of LMOFs should be essential.

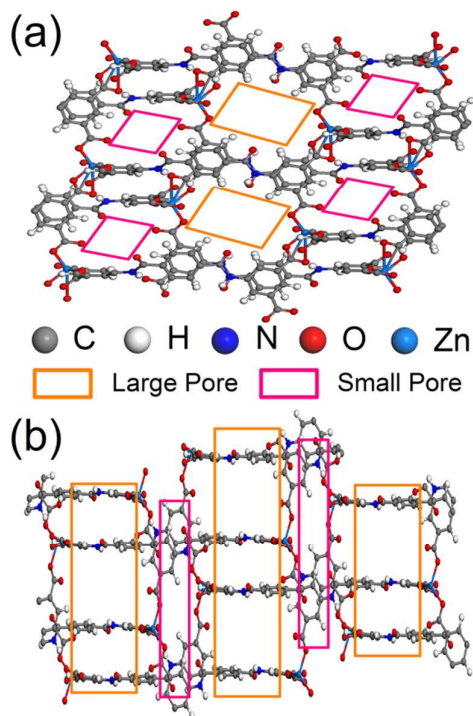


Figure 1. Structural features of LMOF 1. Top view (a); side view (b).

LMOF $\text{Zn}(\text{L})(\text{HDMA})_2(\text{DMF})(\text{H}_2\text{O})_6$ (1) ($\text{H}_4\text{L}=\text{bis}-(3,5\text{-dicarboxy-phenyl})\text{terephthalamide}$), a typical and newly synthesized LMOF has been reported by Wang and co-workers⁴⁴ to show good ability in sensing nitroaromatics (Figure 1, detailed structural information in reference 44). The strong emission of LMOF 1 is remarkably quenched by nitrobenzene while unaffected by alcohols, ketones, chloroalkanes and even other aromatic compounds. This luminescence quenching phenomenon of LMOFs in the presence of nitroaromatics is very useful in explosives-detection and syntheses of quite a few analogous

frameworks have been reported.³⁶⁻⁴⁸ Taking the electron-withdrawing nature of nitroaromatics into consideration, this kind of luminescence quenching is generally attributed to the photo-induced electron transfer from the valence bands (VB) to the conduction bands (CB) of the electron-rich MOF then to the LUMO of the electron-deficient nitroaromatics.^{36-39,49} The positive energy gap between CB and LUMO drives this electron transfer process. This mechanism is quite reasonable but somewhat too brief. As a typical optic sensor, its interaction with the analyte molecule should be the most vital factor that directly affects the intermolecular electron transfer process. Without considerable intermolecular interactions, electron transfer is not likely to occur even in the presence of proper driving forces.³⁶ As is known, electron transfer would be greatly favored via molecular orbital overlap between donor and acceptor.⁵⁰⁻⁵² This kind of overlap is facilitated by intermolecular weak forces which have been studied in the cases of small fluorophores as well as bio-molecules.⁵³⁻⁶⁰ In the cases of LMOFs, to our surprise, this issue has been barely studied.

Hydrogen bond and π - π stacking are the most fundamental and widespread weak interactions. Hydrogen bonds play essential roles in the photo-physical and photo-chemical processes which are closely related to the fluorescence emission quenching/enhancing, intersystem crossing and photo induced proton/electron transfer processes from small organic dyes to complicated metal-organic clusters.^{53-57,61-67} π - π stacking interactions have been demonstrated to facilitate electron transfer in DNAs, metal-organic complexes and so on.⁵⁸⁻⁶⁰ In the cases of LMOFs, their ligands usually contain potential hydrogen bonding sites as well as π - π stacking sites. Nitroaromatics contain nitro groups as hydrogen accepting sites and phenyl rings as π - π stacking sites. When nitroaromatics interact with LMOFs, these two weak forces may coexist. These two interactions will influence the intermolecular electron transfer processes and ultimately coordinate the luminescent properties of LMOFs. However, little is known about the roles of the two weak forces during the luminescent sensing processes of LMOFs. Also, which of them plays a more significant role still remains uncovered.

Based on the above considerations, we perform comprehensive studies on the explosives-detection mechanism of LMOF 1 by using DFT and TD-DFT methods. The interactions between 1 and two analytes from two molecular groups (benzene as hydrocarbon, nitrobenzene as nitroaromatic) are studied. Periodic models are used to study the adsorption of analytes as well as their effects on the electronic structures of LMOF 1. Cluster models are then employed to further look into the electronic couplings between the analytes and sensor.

Methods

For the geometry optimization and single point energy calculation of the periodic structures, all the calculations are performed using the CASTEP⁶⁸ module implemented in the Material Studio 6.0 program suite. DFT calculations are performed using periodic plane-wave methods with a kinetic energy cutoff of 600 eV. The exchange-correlation functional is treated within the generalized gradient approximation (GGA) parametrized by Perdew, Burke, and Ernzerhof (PBE).⁶⁹ Ultrasoft pseudo-potentials are applied throughout the computation. A criterion of 5.0×10^{-7} eV/atom is placed on the self-consistent convergence of the total energy. Atomic positions are considered converged until forces are less than 0.01 eV/Å. Firstly, the unit cell structure of LMOF 1 is fully optimized with the Brillouin-zone sampling restricted to the Γ point. The calculated lattice parameters are in good agreement with the experimental data⁴⁴ (Table S1, Supporting Information) which confirms the validity of our computational methods. Then, unit cell of LMOF 1 is doubled in the b direction and optimized to get the supercell structure before simulating the adsorption of different analytes. Two different analytes namely benzene and nitrobenzene are put inside the large pores of LMOF 1. Nitrobenzene is found to have two potential binding sites inside the pores (namely site 1 and site 2) which lead to two different binding patterns after optimization. These supercell structures optimizations are carried out with respect to all atomic positions considering fixed lattice parameters and brillouin-zone sampling are restricted to the Γ point. Analyte-sensor interaction energies are then calculated using the following equations:

$$E_{\text{interaction}} = E_{\text{LMOF}} + E_{\text{analyte}} - E_{\text{LMOF+analyte}} \quad (1)$$

For all the calculations, dispersion corrections are systematically included to energies and geometries (forces) within the DFT-D method of Grimme.⁷⁰ Local density of states (LDOS) projected on the analytes are then performed based on the optimized structures with the k-point grid of $2 \times 2 \times 1$ (this setting is found to be adequate to give preliminary insights into the electronic coupling between analytes and sensor) using

the Monkhorst-Pack scheme. In order to further test the performance of our theoretical methods, GGA/PW91⁷¹ functional is also applied in the unit cell optimization with the same settings.

For the clusters calculations, we have first investigated the excitation processes by calculating the low-lying excitation energies for all the clusters using TD-DFT method as implemented in Gaussian 09 software package.⁷² Molecular orbitals correlated to the excitation processes are then analyzed from the view of fragment orbital interactions. The fragment orbitals involved in the excited processes are thus obtained. Wavefunctions of these fragment orbitals are generated and multiplied with each other using Multiwfn 3.2.1 program⁷³⁻⁷⁴ to obtain the intermolecular orbital overlap integral values between analytes and the framework. The overlap value can reflect the electronic coupling between the two orbitals and is used in this contribution to visually and quantitatively measure the intermolecular interactions between MOF and nitrobenzene. All the above calculations are performed at the wb97xd⁷⁵/genecp level of theory with the self-consistent reaction field (SCRF) method in a polarizable continuum model (PCM) with acetonitrile as solvent.⁷⁶⁻⁷⁷ The LanL2dz⁷⁸(Zn) /6-31G**(C, H, O, N) basis set are used throughout. Wb97xd⁷⁵ functional is a long-range corrected hybrid functional including empirical dispersion which has given very good performances when dealing with weak intermolecular interactions such as hydrogen bonding and π - π stacking interactions.⁷⁹⁻⁸¹ Thus, we have enough confidence that the level of theory used for the clusters calculations is good enough.

Results and Discussions

An Overview of the LMOF 1 Structure

Having a good understanding of the crystal structure of the MOF sensor, especially the potential binding sites for analytes, will be essential before looking into the detailed sensing mechanism. As shown in Figure 1, each Zn is coordinated with four oxygen atoms from the linkers. Two kinds of pores are formed with different pore sizes. The small pores are rather jammed which will not provide enough space for the adsorption of analytes. On the contrary, the large pores show enough space for analyte adsorption. As revealed in Figure 1, the large pores contain imide groups and phenyl rings which provide possible binding sites for analytes. Thus, analyte-sensor interactions inside these pores should be investigated.

Binding Models and Binding Energies of Different Analytes

Herein, we perform full investigations on the analyte-sensor interactions inside the large pores by using benzene and nitrobenzene as analytes. DFT-D methods are used throughout the optimization of the “analyte-containing” supercell structures. Three binding models are obtained after optimizations, one for the binding of benzene (Ben-MOF) the other two for the bindings of nitrobenzene (NB1-MOF, NB2-MOF). Subsequently, the binding energy of each binding model is obtained (Table 1). As shown in Figure 2a, the interaction between MOF and benzene is of π - π stacking feature with a centroid distance of 3.38 Å. This may provide chances of intermolecular electron transfer. However, the binding energy is quite small (0.764 eV) due to the lack of intermolecular hydrogen bonds. Also, the electron-rich nature of benzene will prohibit the electron transfer process. Thus, benzene would not quench the luminescence of LMOF 1 which is in accordance with the experimental results.

Table 1. Binding energies for the three binding models.^a

Structure	Binding Energy (eV)
Ben-MOF	0.764
NB1-MOF	0.995
NB2-MOF	0.959

^aDetailed information of the binding energies have been listed in Table S3 (Supporting Information).

In the case of nitrobenzene, two binding patterns are present inside the large pore. Figure 2b shows the NB1-MOF binding model (binding site 1). A strong hydrogen bond (1.81 Å) and a moderate hydrogen bond (2.54 Å) form between the analyte and sensor. The total binding energy for this model is 0.995 eV, considerably larger than that of Ben-MOF. The other binding model (NB2-MOF, binding site 2), as revealed in Figure 2c, shows the co-existence of a moderate hydrogen bond (2.62 Å) and a π - π stacking interaction (centroid distance 3.44 Å). Binding energy for this model is 0.959 eV, which is close to the case of NB1-MOF. The large binding energies of NB1-MOF and NB2-MOF indicate strong analyte-sensor binding strengths. This may increase the degree of electronic coupling between the analyte and

sensor which facilitates the electron transfer and induces the experimentally observed luminescence quenching. Thus, the electronic couplings between the analytes and sensor should be investigated.

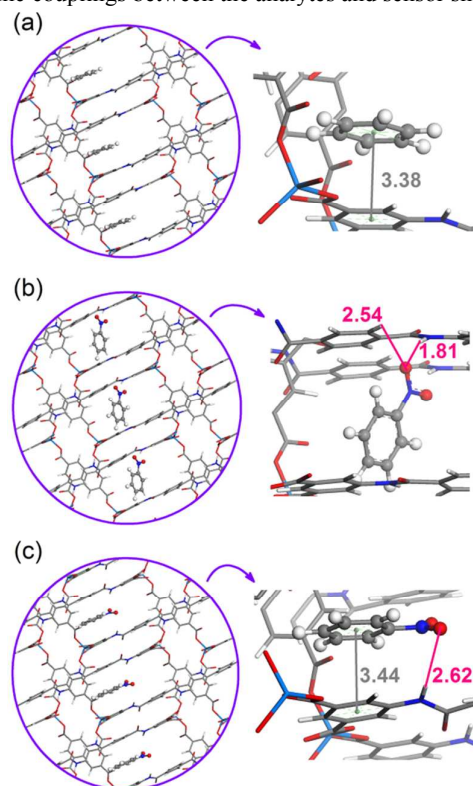


Figure 2. Geometries of LMOF 1 optimized by DFT-D calculations for the adsorption of (a) benzene, (b) nitrobenzene on site 1 and (c) nitrobenzene on site 2. Right sides are the corresponding magnifications. Hydrogen bond lengths and centroid distances between aromatic rings are given. All the distances units are in Angstrom (Å).

A Primary View of the Electronic Coupling

A preliminary view of the electronic couplings between the analytes and sensor is indicated by calculating the electronic density of states (DOS) as well as local density of states (LDOS) projected onto the adsorbates. As displayed in Figure 3b, the adsorption of benzene into the pores of LMOF 1 induces a clear overlap of the main peak in the region $-1-0$ eV. This indicates that the occupied frontier orbitals of benzene may have strong interactions with the top VB of LMOF 1. However, there are no obvious overlap zones in the regions of CB. This will make the electron transfer from CB to LUMO hard to take place which further confirms that benzene cannot quench the luminescence of LMOF 1.

For the cases of nitrobenzene, the two binding models exhibit very similar DOS/LDOS diagrams. As shown in Figure 3c and 3d, the adsorptions of nitrobenzene into the two sites all bring about overlaps near the first main peaks in the VB zones. Besides, new peaks appear just around the bottom of the CB of the framework (in region $1.8-2.5$ eV) for both cases, indicating the possible existence of strong interactions between the frontier unoccupied orbitals of the analyte (nitrobenzene) and bottom CB of the sensor (LMOF 1). Thus, we can get that, the electronic structure of LMOF 1 is quite sensitive for the presence of nitrobenzene. The strong electronic coupling between nitrobenzene and LMOF 1 increases the chances of electron transfer from CB to LUMO which consequently induces luminescence quenching.

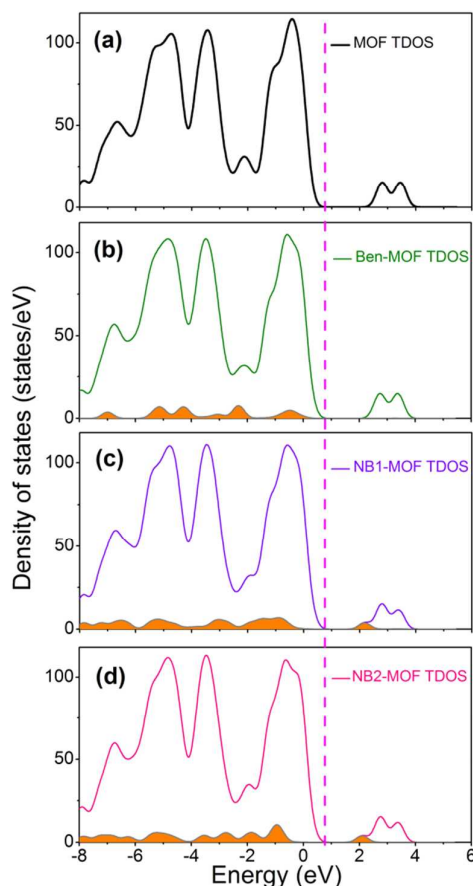


Figure 3. The total electronic density of states (TDOS) for (a) LMOF 1, (b) Ben-MOF, (c) NB1-MOF and (d) NB2-MOF. The local DOS projected onto the analytes are also plotted (filled areas under DOS curves).

As discussed in the above sections, we have investigated the analyte-sensor interactions from the view of binding models to inherent electronic couplings. The overlap of DOS between the analyte and the framework around the bottom of the CB is found to be a prerequisite for intermolecular electron transfer. Nitrobenzene shows two binding models with LMOF 1. These models have very different intermolecular interactions. NB1-MOF has two hydrogen bonds while NB2-MOF has both hydrogen bonding and π - π stacking interactions. Intermolecular hydrogen bond and π - π stacking seem to facilitate this electronic coupling and play important roles. As hydrogen bond and π - π stacking are intrinsically different in bonding patterns and electronic interactions, the different binding models of nitrobenzene with LMOF 1 may induce very different intermolecular electron transfer features. However, both the analyses of bonding energies and DOS cannot distinguish these two binding models. To get a detailed picture on how these two weak forces function and which of them plays a more significant role during the electron transfer process, we take further steps into the electronic properties of the above mentioned structures. In the sections below, cluster models of these structures have been applied to study these issues.

Descriptions of the Cluster Models

In the studies of infinite MOFs crystal structures, truncated cluster models from the periodic structures have been successfully applied.⁸²⁻⁸⁹ The finite clusters should be delicately selected to best represent their original local chemical environment. In this contribution, four clusters namely CL-LMOF 1, CL-Ben-MOF, CL-NB1-MOF and CL-NB2-MOF are obtained by truncating from the corresponding optimized periodic structures. H atom is used to balance the overall charges such that the truncated clusters remain neutral. Detailed truncating procedures are given in Figure S1 (Supporting Information). Truncated structures are shown in Figure S2 (Supporting Information).

Analyses of the Excitation Processes

Excitations of LMOFs from ground states to electronic excited states frequently trigger electron transfer. The presence of analyte molecules would affect these electron transfer processes and induce changes of luminescence. Thus, a good understanding of the excitation process will provide useful insights into the luminescence quenching mechanism of LMOF 1. Herein, TD-DFT calculations are performed to investigate the excitation processes using the cluster models. Based on the fact that the emission spectra are obtained by exciting the samples at the 330 nm absorption peak,⁴⁴ the electronic transition states around this excitation wavelength are studied. Detailed information on the excitation processes have been given in Table S4 (Supporting Information).

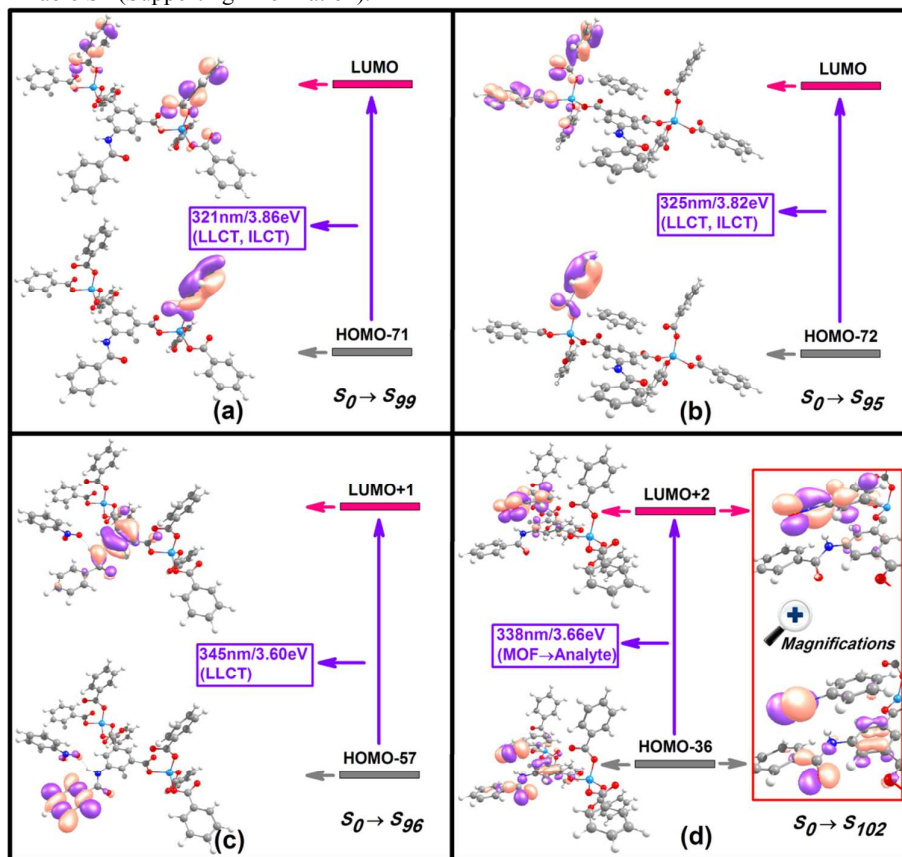


Figure 4. Molecular orbitals involved in the excitation processes for (a) CL-LMOF 1, (b) CL-Ben-MOF, (c) CL-NB1-MOF and (d) CL-NB2-MOF. Corresponding excitation wavelengths/energies and excitation features are shown in this picture. LLCT represents ligand to ligand charge transfer. ILCT represents intra-ligand charge transfer. “MOF→Analyte” represents electron transfer from MOF to analyte molecule.

As shown in Figure 4a, the excitation of LMOF 1 at 330 nm in the experiment corresponds to the $S_0 \rightarrow S_{99}$ electronic transition (calculated value at 321 nm) of the corresponding cluster model. This transition exhibits ligand to ligand charge transfer (LLCT) feature coupled with intra-ligand charge transfer (ILCT) feature, indicating the excitation of LMOF 1 is linker based. For the case of Ben-MOF, the excitation at 330 nm corresponds to the $S_0 \rightarrow S_{95}$ (calculated value 325 nm) electronic transition. The molecular orbitals involved in the excitation (HOMO-72, LUMO) show that this process still localizes inside the MOF structure (LLCT, ILCT). This is further confirmed by the molecular orbital composition analyses. As shown in Figure S3 (Supporting Information), LUMO of the cluster is mainly (99.7%) composed of the LUMO of the framework. Thus, benzene does not participate during the excitation process which is in accordance with the LDOS results (no overlaps are observed between the unoccupied orbitals of benzene and CB of MOF). Also, the LUMO energy of benzene is much higher than that of LMOF 1 owing to its electron-rich nature (Figure S3, Supporting Information). All these results demonstrate that benzene cannot accept the electrons from LMOF 1 which brings negligible effects on LMOF 1's luminescence.

The case of nitrobenzene may be quite different as nitrobenzene usually serves as a good electron acceptor. However, as revealed in Figure 4c, the excitation process of the NB1-MOF cluster features LLCT. Nitrobenzene is not involved in the excitation process with this “pure hydrogen binding model”. For the NB2-MOF cluster (Figure 4d), the excitation of this “hybrid binding model” exhibits a clear electron transfer process from LMOF 1 to nitrobenzene. As shown in Figure S4 and Figure S5 (Supporting Information), LUMO energy of nitrobenzene is very close to the unoccupied orbital of LMOF 1 (MOF fragment orbital 278 in both cases) for both models. Nevertheless, the electron transfer processes are essentially different. This disparity may originate from the different nature of hydrogen bond and π - π stacking which leads to different analyte-sensor interactions. To give an intuitive study on the effects of the two intermolecular interactions, the compositions of the molecular orbitals involved in the excitation processes (HOMO-57 and LUMO+1 for CL-NB1-MOF, HOMO-36 and LUMO+2 for CL-NB2-MOF) are analyzed. Overlaps between the fragment orbitals are also investigated in the section below. Motivation for the selection of the molecular orbitals are fully addressed below Table S4 (Supporting Information).

Fragment Orbital Compositions and Intermolecular Orbital Overlaps

Firstly, we have investigated the compositions of the molecular orbitals involved in the excitation processes. The CL-NB2-MOF structure is divided into two fragments namely the MOF fragment and the NB2 (nitrobenzene) fragment. Consequently, we obtain the fragment orbitals interaction diagram (see detailed information in Figure S4, Supporting Information) between the two fragments. Compositions of the molecular orbitals related to the $S_0 \rightarrow S_{102}$ electronic transition (orbital number 270, 309) are analyzed. As shown in Figure 5a, the 309 unoccupied molecular orbital is composed from two fragment orbitals. MOF fragment orbital 278 contributes 2.2% while NB2 fragment orbital 33 contributes as much as 93.7%. This indicates strong intermolecular electron transfer occurs from MOF to nitrobenzene with this “hybrid binding model”. The 278 fragment orbital and the 33 fragment orbital are closely related to the electron transfer process. The corresponding orbitals are also plotted in Figure 5a. Both fragment orbital 278 and fragment orbital 33 exhibits π^* features. These two fragments are close in space with the aromatic rings nearly parallel to each other. This would significantly render fragment orbital overlaps between 278 and 33 which facilitate intermolecular electron transfer. Herein, this overlap integral value is obtained which is as large as 0.0121. Also, the overlapping zones are visually obtained and shown in Figure 5b. π - π stacking are found to be the main factors which facilitates the electron transfer process as the overlapping zones between 278 and 33 mainly locate between the two aromatic rings. Besides, the overlap is also present at the hydrogen bonding zone. This indicates hydrogen bonding interaction also facilitates intermolecular electron transfer but is not the major factor. Based on the above analyses, intermolecular electron transfer from CB of MOF to LUMO of nitrobenzene is proved to be a fairly favorable process.

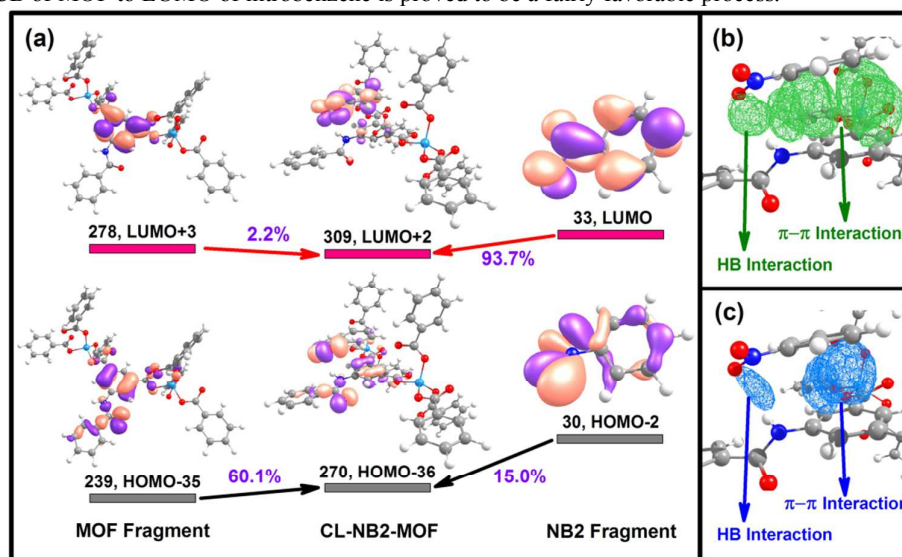


Figure 5. (a) Fragment orbital interaction diagram for CL-NB2-MOF. Intermolecular orbital overlap zone between (b) 278 orbital of fragment MOF and 33 orbital of fragment NB; (c) 239 orbital of fragment MOF and 30 orbital of fragment NB. The green surfaces represent the overlap zones between unoccupied

fragment orbitals and the blue surfaces represent the overlap zones between occupied fragment orbitals. Contour value for the orbital overlaps is set to 0.00002.

The occupied molecular orbital 270 is also composed from these two fragments. MOF fragment orbital 239 contributes 60.1% and NB2 fragment orbital 30 contributes 15.0%. This indicates a strong electronic coupling between 239 and 30 which may also induce intermolecular transfer between the two fragments. In this case, electrons may be directly photo-excited from VB of MOF to the LUMO of nitrobenzene. As plotted in Figure 5a, the 239 fragment orbital has mixed features. The aromatic ring in the middle shows a clear π feature whereas the imide group shows an n feature. Likewise, for fragment orbital 30, the aromatic ring shows a π feature and the nitro group shows an n feature. Thus, we can expect the π feature would induce overlaps between the aromatic rings while the n feature would induce overlaps between nitro and imide groups. Consequently, the overlap zones are plotted in Figure 5c which is in accordance with the above prediction. However, the overlap integral value is 0.0033, much smaller than that between 278 and 33. Based on this, electrons directly photo-excited from the MOF fragment to LUMO of nitrobenzene is quite unlikely to happen.

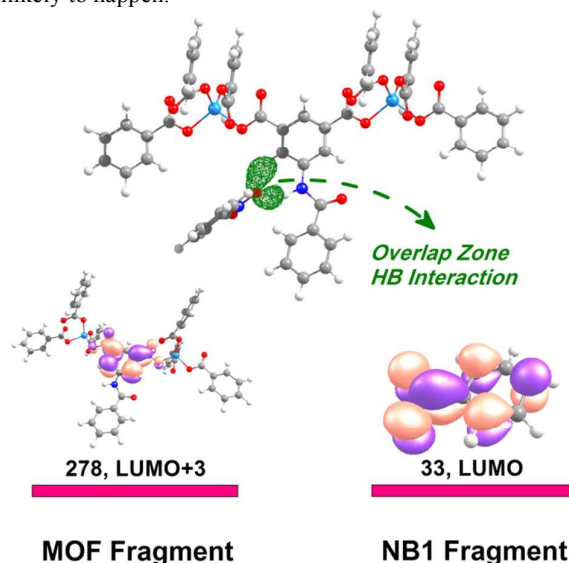


Figure 6. Fragment orbital overlap between 278 orbital of MOF fragment and 33 orbital of NB1 fragment. Contour value for the orbital overlaps is set to 0.00002.

Compositions of the molecular orbitals involved in the $S_0 \rightarrow S_{96}$ excitation process (orbital number 249 and 308) of CL-NB1-MOF are then investigated. In this case, both the 249 orbital and 308 orbital are solely composed from the fragment orbitals of the MOF fragment. As shown in Figure S5 (Supporting Information), MOF fragment orbital 223 contributes 97.2% for the 249 molecular orbital. MOF fragment orbital 276 contributes 94.5% for the 308 molecular orbital. These indicate that the “pure hydrogen bonding model” is not favorable in transferring electrons. To provide further evidence, the fragment orbital overlap between the MOF fragment orbital 278 and NB1 fragment orbital 33 are obtained and shown in Figure 6. The overlaps are found to locate at the two hydrogen bonding zones with an integral value of 0.0018. This value is much smaller than the case of the “hybrid binding model”, suggesting hydrogen bond, alone, cannot provide enough overlaps for intermolecular electron transfer.

From the orbital overlap analyses we can conclude that hydrogen bond is less efficient for electron transfer due to the small overlap values. On the contrary, π - π stacking shows higher efficiency for electron transfer. π - π stacking interaction seems to outperform hydrogen bonding interaction in the explosive detecting process of nitrobenzene with this MOF sensor. However, as revealed by the binding energies (Table 1), the “hybrid bonding model” has a binding energy 0.2 eV larger than that of Ben-MOF. This “extra binding strength” is originated from the hydrogen bond, which increases the chances of nitrobenzene binding to the MOF sensor. Thus, hydrogen bond, although less efficient in electron transfer, cooperates with the π - π stacking. The collaboration of the two interactions induces strong luminescence quenching and achieves the detection of explosives.

Conclusions

To sum up, the explosives detecting mechanism for LMOF 1 has been comprehensively studied by analyzing the analyte-sensor interactions. Nitrobenzene-induced luminescence quenching of LMOF 1 is demonstrated to stem from the intermolecular electron transfer from the MOF sensor to the analyte. The electrons transfer from the CB of the MOF to the LUMO of nitrobenzene upon photo-excitation due to the electron withdrawing ability of nitrobenzene. Intermolecular interactions between the framework and nitrobenzene are found to play essential roles in this electron transfer process which are directly responsible for the luminescence quenching of LMOF 1. π - π stacking interaction provides large overlaps between the analyte and sensor which serves as the electron transfer bridge. Hydrogen bond, alone, cannot provide enough overlaps for electron transfer but is found to reinforce the π - π stacking interaction. The cooperation of the two interactions leads to significant luminescence quenching of LMOF 1 in the presence of nitrobenzene. In the design of nitroaromatics-detecting MOF sensors, the analyte-sensor interaction can be optimized by introducing hydrogen binding sites (namely imide group, amino group) as well as π - π stacking sites into the MOF ligands. This provides a piece of useful guidance for the experimentalists.

Acknowledgments

The authors would like to thank the National Natural Science Foundation of China for the financial support (Grant Nos. 21137001, 21036006, 21373042).

Notes and references

^a State Key Laboratory of Fine Chemicals, Dalian University of Technology, Dalian 116024, China. haoce@dlut.edu.cn

^b State Key Laboratory of Molecular Reaction Dynamics, Dalian Institute of Chemical Physics, Chinese Academy of Sciences, Dalian 116023, China.

The authors declare no competing financial interest.

Electronic Supplementary Information (ESI) available: [Figure S1 shows the truncating of the cluster models; Figure S2 shows the structure of the cluster models. Figure S3 Figure S4 and Figure S5 show the detailed information of the fragment orbital interactions between the framework and analytes. Table S1 shows the calculated crystal lattice parameters as well as the corresponding experimental data. Table S2 tests the selecting of k-points. Table S3 gives the binding energies for the adsorbates in detail. Table S4 reports the calculated excitation energies for the clusters.

References and Notes

1. O. M. Yaghi, M. O'Keeffe, N. W. Ockwig, H. K. Chae, M. Eddaoudi and J. Kim, *Nature*, 2003, 423, 705–714.
2. S.L. James, *Chem. Soc. Rev.* **2003**, 32, 276–288.
3. S. Kitagawa, R. Kitaura and S. Noro, *Angew. Chem., Int. Ed.*, 2004, 43, 2334–2375.
4. J. R. Long and O. M. Yaghi, *Chem. Soc. Rev.*, 2009, 38, 1213–1214.
5. H. C. Zhou, J. R. Long and O. M. Yaghi, *Chem. Rev.*, 2012, 112, 673–674.
6. M. Eddaoudi, J. Kim, N. Rosi, D. Vodak, J. Wachter, M. O'Keeffe and O. M. Yaghi, *Science*, 2002, 295, 469–472.
7. J. Rowsell and O. M. Yaghi, *Angew. Chem., Int. Ed.*, 2005, 44, 4670–4679.
8. W. Zhou and T. Yildirim, *J. Phys. Chem. C*, 2008, 112, 8132–8135.
9. T. A. Makal, J. R. Li, W. Lu and H. C. Zhou, *Chem. Soc. Rev.*, 2012, 41, 7761–7779.
10. A. Demessence and J. R. Long, *Chem. Eur. J.*, 2010, 16, 5902–5908.
11. J. R. Li, J. Sculley and H. C. Zhou, *Chem. Rev.*, 2012, 112, 869–932.
12. Q. Yang, D. Liu, C. Zhong and J. R. Li, *Chem. Rev.*, 2013, 113, 8261–8323.
13. P. Horcajada, C. Serre, M. Vallet-Regí, M. Sebban, F. Taulelle and G. Férey, *Angew. Chem. Int. Ed.*, 2006, 118, 6120–6124.
14. J. Lee, O. K. Farha, J. Roberts, K. A. Scheidt, S. T. Nguyen and J. T. Hupp, *Chem. Soc. Rev.*, 2009, 38, 1450–1459.
15. D. Dang, P. Wu, C. He, Z. Xie and C. Duan, *J. Am. Chem. Soc.*, 2010, 132, 14321–14323.
16. Z. Xie, C. Wang, K. E. DeKrafft and W. Lin, *J. Am. Chem. Soc.*, 2011, 133, 2056–2059.
17. L. Yang, P. Vajeeston, P. Ravindran, H. Fjellvåg and M. Tilset, *Inorg. Chem.*, 2010, 49, 10283–10290.
18. L. Yang, P. Vajeeston, P. Ravindran, H. Fjellvåg and M. Tilset, *Phys. Chem. Chem. Phys.*, 2011, 13, 10191–10203.
19. L. Yang, P. Vajeeston, P. Ravindran and M. Tilset, *RSC Adv.*, 2012, 2, 1618–1631.
20. L. Yang, P. Ravindran, P. Vajeeston and M. Tilset, *Phys. Chem. Chem. Phys.*, 2012, 14, 4713–4723.
21. L. Yang, P. Ravindran, P. Vajeeston and M. Tilset, *J. Mater. Chem.*, 2012, 22, 16324–16335.
22. L. Yang, P. Ravindran and M. Tilset, *Inorg. Chem.*, 2013, 52, 4217–4228.

23. L. Yang, P. Ravindran, P. Vajeeston, S. Svelle and M. Tilset, *Microporous Mesoporous Mater.*, 2013, 175, 50–58.
24. L. Yang, *Microporous Mesoporous Mater.*, 2014, 183, 218–233.
25. L. Yang, G. Fang, J. Ma, E. Ganz and S. S. Han, *Cryst. Growth Des.*, 2014, 14, 2532–2541.
26. L. Yang, E. Ganz, S. Svelle and M. Tilset, *J. Mater. Chem. C*, 2014, 2, 7111–7125
27. J. Gascon, M. D. Hernández-Alonso, A. R. Almeida, G. P. M. van Klink, F. Kapteijn and G. Mul, *ChemSusChem*, 2008, 1, 981–983.
28. M. D. Allendorf, C. A. Bauer, R. K. Bhakta, and R. J. T. Houk, *Chem. Soc. Rev.*, 2009, 38, 1330–1352.
29. Y. Cui, Y. Yue, G. Qian and B. Chen, *Chem. Rev.*, 2012, 112, 1126–1162.
30. Y. Cui, H. Xu, Y. Yue, Z. Guo, J. Yu, Z. Chen, J. Gao, Y. Yang, G. Qian and B. Chen, *J. Am. Chem. Soc.*, 2012, 134, 3979–3982.
31. J. C. G. Bunzli and C. Piguet, *Chem. Soc. Rev.*, 2005, 34, 1048–1077.
32. B. L. Chen, S. Xiang and G. Qian, *Acc. Chem. Res.*, 2010, 43, 1115–1124.
33. L. E. Kreno, K. Leong, O. K. Farha, M. Allendorf, D. R. P. Van and J. T. Hupp, *Chem. Rev.*, 2012, 112, 1105–1125.
34. B. Liu, *J. Mater. Chem.*, 2012, 22, 10094–10101.
35. Z. C. Hu, B. J. Deibert and J. Li, *Chem. Soc. Rev.* 2014, DOI: 10.1039/c4cs00010b.
36. S. C. Pramanik, X. Zheng, T. Zhang, J. Emge and J. Li, *J. Am. Chem. Soc.*, 2011, 133, 4153–4155.
37. D. Banerjee, Z. Hu, S. Pramanik, X. Zhang, H. Wang and J. Li, *CrystEngComm*, 2013, 15, 9745–9750.
38. B. Gole, A. K. Bar and P. S. Mukherjee, *Chem. Eur. J.*, 2014, 20, 2276–2291.
39. G. L. Liu, Y. J. Qin, J. Li, G. Y. Wei and H. Li, *Chem. Commun.*, 2013, 49, 1699–1701.
40. A. Lan, K. Li, H. Wu, D. H. Olson, T. J. Emge, W. Ki, M. Hong and J. Li, *Angew. Chem. Int. Ed.*, 2009, 48, 2334–2338.
41. A. Lan, K. Li, H. Wu, L. Kong, N. Nijem, D. H. Olson, T. J. Emge, Y. J. Chabal, D. C. Langreth, M. Hong and J. Li, *Inorg. Chem.*, 2009, 48, 7165–7173.
42. G. Y. Wang, L. L. Yang, Yue. Li, H. Song, W. J. Ruan, Z. Chang and X. H. Bu, *Dalton Trans.*, 2013, 42, 12865–12868.
43. D. X. Ma, B. Y. Li, X. J. Zhou, Q. Zhou, K. Liu, G. Zeng, G. H. Li, Z. Shi and S. H. Feng, *Chem. Commun.*, 2013, 49, 8964–8966.
44. G. Y. Wang, C. Song, D. M. Kong, W. J. Ruan, Z. Chang and Y. Li, *J. Mater. Chem. A*, 2014, 2, 2213–2220.
45. Z. Feng, W. B. Tan, M. L. Feng, A. J. Lana and X. Y. Huang, *J. Mater. Chem. A*, 2014, 2, 6426–6431.
46. B. L. Chen, S. Ma, F. Zapata, E. B. Lobkovsky and J. Yang, *Inorg. Chem.*, 2006, 45, 5718–5720.
47. T. K. Kim, J. H. Lee, D. Moon and H. R. Moon, *Inorg. Chem.*, 2013, 52, 589–595.
48. Z. Hu, S. Pramanik, K. Tan, C. Zheng, W. Liu, X. Zhang, Y. J. Chabal and J. Li, *Cryst. Growth Des.*, 2013, 13, 4204–4207.
49. S. Pramanik, Z. Hu, X. Zhang, C. Zheng, S. Kelly and J. Li, *Chem. Eur. J.*, 2013, 19, 15964–15971.
50. L. Lawrence and H. Roald, *J. Am. Chem. Soc.*, 1974, 96, 1370–1383.
51. L. C. Gerhard, P. Piotr, M. M. Jean and R. F. Graham, *J. Am. Chem. Soc.*, 1988, 110, 2652–2653.
52. G. Fruszina, V. Siim, H. Felix, S. Jacob, B. Marian, K. Adam, D. Michel and B. Jochen, *J. Chem. Theory Comput.*, 2014, DOI: 10.1021/ct500527v.
53. P. J. Rege, S. A. Williams and M. J. Therien, *Science*, 1995, 269, 1409–1413.
54. G. J. Zhao, J. Y. Liu, L. C. Zhou and K. L. Han, *J. Phys. Chem. B*, 2007, 111, 8940–8945.
55. A. P. Demchenko, K. C. Tang and P. T. Chou, *Chem. Soc. Rev.*, 2013, 42, 1379–1408.
56. D. R. Weinberg, C. J. Gagliardi, J. F. Hull, C. F. Murphy, C. A. Kent, B. C. Westlake, A. Paul, D. H. Ess, D. G. McCafferty and T. J. Meyer, *Chem. Rev.*, 2012, 112, 4016–4093.
57. O. S. Wenger, *Acc. Chem. Res.*, 2013, 46, 1517–1526.
58. D. B. Hall, R. E. Holmlin and J. K. Barton, *Nature*, 1996, 382, 731–735.
59. S. O. Kelley and J. K. Barton, *Chem. Bio.*, 1998, 5, 413–425.
60. J. Christoph, *J. Chem. Soc., Dalton Trans.*, 2000, 3885–3896.
61. G. J. Zhao and K. L. Han, *Acc. Chem. Res.*, 2012, 45, 404–413.
62. K. L. Han and G. J. Zhao, *Hydrogen Bonding and Transfer in the Excited State*; John Wiley & Sons Ltd.: Chichester, U.K., 2011; Vol. I & II.
63. G. J. Zhao and K. L. Han, *J. Phys. Chem. A*, 2009, 113, 14329–14335.
64. Y. H. Liu and S. C. Lan, *Commun. Comput. Chem.*, 2013, 3, 235–243.
65. D. P. Yang, Y. G. Yang and Y. F. Liu, *Commun. Comput. Chem.*, 2013, 3, 205–215.
66. Y. H. Liu and S. C. Lan, *Commun. Comput. Chem.*, 2013, 1, 1–7.
67. N. Agmon, *J. Phys. Chem. A*, 2005, 109, 13–35.

68. S. J. Clark, M. D. Segall, C. J. Pickard, P. J. Hasnip, M. J. Probert, K. Refson and M. C. Z. Payne, *Z. Kristallogr.*, 2005, 220, 567–570.
69. J. Perdew, K. Burke and M. Ernzerhof, *Phys. Rev. Lett.*, 1996, 77, 3865.
70. S. Grimme, *J. Comput. Chem.*, 2006, 27, 1787–1799.
71. J. P. Perdew, J. A. Chevary, S. H. Vosko, K. A. Jackson, M. R. Pederson, D. J. Singh and C. Fiolhais, *Phys. Rev. B*, 1992, 46, 6671–6687.
72. M. J. Frisch, G. W. Trucks, H. B. Schlegel, G. E. Scuseria, M. A. Robb, J. R. Cheeseman, G. Scalmani, V. Barone, B. Mennucci, G. A. Petersson, H. Nakatsuji, M. Caricato, X. Li, H. P. Hratchian, A. F. Izmaylov, J. Bloino, G. Zheng, J. L. Sonnenberg, M. Hada, M. Ehara, K. Toyota, R. Fukuda, J. Hasegawa, M. Ishida, T. Nakajima, Y. Honda, O. Kitao, H. Nakai, T. Vreven, J. A., Jr. Montgomery, J. E. Peralta, F. Ogliaro, M. Bearpark, J. J. Heyd, E. Brothers, K. N. Kudin, V. N. Staroverov, R. Kobayashi, J. Normand, K. Raghavachari, A. Rendell, J. C. Burant, S. S. Iyengar, J. Tomasi, M. Cossi, N. Rega, N. J. Millam, M. Klene, J. E. Knox, J. B. Cross, V. Bakken, C. Adamo, J. Jaramillo, R. Gomperts, R. E. Stratmann, O. Yazyev, A. J. Austin, R. Cammi, C. Pomelli, J. W. Ochterski, R. L. Martin, K. Morokuma, V. G. Zakrzewski, G. A. Voth, P. Salvador, J. J. Dannenberg, S. Dapprich, A. D. Daniels, Ö. Farkas, J. B. Foresman, J. V. Ortiz, J. Cioslowski and D. J. Fox, Gaussian 09, revision C.01; Gaussian, Inc.: Wallingford, CT, 2009.
73. T. Lu and F. W. Chen, *J. Comput. Chem.*, 2012, 33, 580–592.
74. T. Lu, F. W. Chen and W. Chen, *J. Mol. Graphics Modell.*, 2012, 38, 314–323.
75. J. Chai and M. H. Gordon, *J. Chem. Phys.*, 2008, 128, 084106.
76. S. Miertuš, E. Scrocco and J. Tomasi, *Chem. Phys.*, 1981, 55, 117–129.
77. R. Cammi and J. Tomasi, *J. Comput. Chem.*, 1995, 16, 1449–1458.
78. P. J. Hay and W. R. Wadt, *J. Chem. Phys.*, 1985, 82, 299–310.
79. P. Gu, R. Q. Lu, D. Liu, Y. K. Lu and S. T. Wang, *Phys. Chem. Chem. Phys.*, 2014, 16, 10531–10538.
80. T. B. Tai and M. T. Nguyen, *Chem. Commun.*, 2013, 49, 913–915.
81. S. Panigrahi, A. Bhattacharya, S. Banerjee and D. Bhattacharyya, *J. Phys. Chem. C*, 2012, 116, 4374–4379.
82. L. Grajciar, A. D. Wiersum, P. L. Llewellyn, J. S. Chang and P. Nachtigall, *J. Phys. Chem. C*, 2011, 115, 17925–17933.
83. A. L. Dzubakl, L. C. Lin, J. H. Kim, J. A. Swisher, R. Poloni, S. N. Maximoff, B. Smit and L. Gagliardi, *Nat. Chem.*, 2012, 4, 810–816.
84. M. Ji, X. Lan, Z. P. Han, C. Hao and J. S. Qiu, *Inorg. Chem.*, 2012, 51, 12389–12394.
85. X. Sui, M. Ji, X. Lan, W. H. Mi, C. Hao and J. S. Qiu, *Inorg. Chem.*, 2013, 52, 5742–5748.
86. M. Ji, C. Hao, D. D. Wang, H. Li and J. S. Qiu, *Dalton Trans.*, 2013, 42, 3464–3470.
87. M. X. Zhang, W. H. Mi and C. Hao, *Commun. Comput. Chem.*, 2013, 1, 269–281.
88. S. H. Kang, Z. Q. Liu, J. J. Tan, C. Hao and J. S. Qiu, *Commun. Comput. Chem.*, 2014, 2, 69–87.
89. Y. Yao, X. Song, J. Qiu and C. Hao, *J. Phys. Chem. A*, 2014, 118, 6191–6196.

Table(s)Table 1. Binding energies for the three binding models.^a

Structure	Binding Energy (eV)
Ben-MOF	0.764
NB1-MOF	0.995
NB2-MOF	0.959

^aDetailed information of the binding energies have been listed in Table S3 (Supporting Information).

Figure Captions:

Figure 1. Structural features of LMOF 1. Top view (a); side view (b).

Figure 2. Geometries of LMOF 1 optimized by DFT-D calculations for the adsorption of (a) benzene, (b) nitrobenzene on site 1 and (c) nitrobenzene on site 2. Right sides are the corresponding magnifications. Hydrogen bond lengths and centroid distances between aromatic rings are given. All the distances units are in Angstrom (Å).

Figure 3. The total electronic density of states (TDOS) for (a) LMOF 1, (b) Ben-MOF, (c) NB1-MOF and (d) NB2-MOF. The local DOS projected onto the analytes are also plotted (filled areas under DOS curves).

Figure 4. Molecular orbitals involved in the excitation processes for (a) CL-LMOF 1, (b) CL-Ben-MOF, (c) CL-NB1-MOF and (d) CL-NB2-MOF. Corresponding excitation wavelengths/energies and excitation features are shown in this picture. LLCT represents ligand to ligand charge transfer. ILCT represents intra-ligand charge transfer. “MOF→Analyte” represents electron transfer from MOF to analyte molecule.

Figure 5. (a) Fragment orbital interaction diagram for CL-NB2-MOF. Intermolecular orbital overlap zone between (b) 278 orbital of fragment MOF and 33 orbital of fragment NB; (c) 239 orbital of fragment MOF and 30 orbital of fragment NB. The green surfaces represent the overlap zones between unoccupied fragment orbitals and the blue surfaces represent the overlap zones between occupied fragment orbitals. Contour value for the orbital overlaps is set to 0.00002.

Figure 6. Fragment orbital overlap between 278 orbital of MOF fragment and 33 orbital of NB1 fragment. Contour value for the orbital overlaps is set to 0.00002.